Check for updates

Received: 9 September 2023 | Revised: 15 January 2024 | Accepted: 20 January 2024

IET Electric Power Applications

DOI: 10.1049/elp2.12424

The Institution of Engineering and Technology WILEY

ORIGINAL RESEARCH

MaglevMotor: Design and optimisation of a novel hybrid linear actuator for 6 degrees of freedom rail-passive Maglev carrier

Ahmet Fevzi Bozkurt | **Kadir Erkan**

Department of Mechatronics Engineering, Yıldız Technical University, Istanbul, Turkey

Correspondence
Ahmet Fevzi Bozkurt.
Email: afbozkurt90@gmail.com

Abstract

A novel levitating hybrid linear actuator is proposed for magnetically levitated carrier systems. This hybrid linear actuator, "MaglevMotor", is capable to levitate itself under the passive rail and thrusts itself in a single longitudinal direction. The proposed structure aims to reduce complexity by minimising the necessary number of components, resulting in simplified geometry, improved assembly convenience, and decreased manufacturing tolerances. The MaglevMotor is optimised in multi-physics aspect. Optimisation objectives are maximising thrust force, minimising total mass and minimising mechanical deformation of yoke with constraints of a user defined magnetic flux density (B) in yoke and zero power condition for specific air gap value. The authors present pre-optimisation studies, optimisation results and final MaglevMotor designs step by step. By utilising three of the MaglevMotors units, the carrier is able to achieve motion in six degrees of freedom. The carrier's performance targets, including a 0.2 G acceleration, a total mass of less than 10 kg, and a 5 mm levitation air gap, have been both attained and validated through corresponding experiments.

KEYWORDS
hybrid yoke, linear induction motors, magnetic actuators, magnetic levitation, optimisation

1 | INTRODUCTION

Maglev (Magnetic Levitation) technology is gaining popularity in both academic studies and industrial applications. With the benefits of Maglev technology, such as mechanical-contact-free, silent and vibration-free motion, carriers can be developed at clean-room-class across various dimensions, ranging from super-high-speed trains to indoor transportation systems to micro robots can travel inside veins [1–3]. Its frictionless motion capabilities give opportunity to achieve ultra-high speeds and precise motion in transportation systems, also because of the wheel-free design, carrier (or called mover, transporter etc.) is isolated from ground which means no vibration or noise during operation [4]. Taking advantage of these benefits results in a significant decrease in the number of mechanical parts required for the carrier, as the need for extra components such as springs or dampers to address vibration is eliminated. Furthermore, the components employed in Maglev carriers exhibit an extended lifespan due to their tear-free and wear-free operational nature.

A levitating carrier cannot use traditional wheels for translational motion because of contactless attributes. The linear motors are required to solve this problem. The linear motor can be imagined as a conventional rotary motor cut perpendicularly and flattened. With this transition, the rotary motion is also flattened and becomes a direct drive longitudinal motion [5]. This longitudinal motion can be realised through various types of linear motors, including synchronous, asynchronous, tubular and many different types of linear motors [6]. One of the notable examples of linear motors usage is the super high-speed train systems. This [1] method uses the long stator type linear motors for the propulsion system of the train and the other referred method [7] uses same linear motor type but with super conducting windings. As anticipated, this method requires the use of linear motors spanning kilometres along the track. Although powering issue can be covered by

This is an open access article under the terms of the Creative Commons Attribution License, which permits use, distribution and reproduction in any medium, provided the original work is properly cited.

© 2024 The Authors. *IET Electric Power Applications* published by John Wiley & Sons Ltd on behalf of The Institution of Engineering and Technology.

separately driving the segmented rails, long stator motors necessitate both high manufacturing costs and a more complex driving technique. In the domain of indoor transportation, the employment of these long stator motors facilitates precise positioning [8]. Moreover, through this methodology, the primary power consumption, the propulsion system, is transferred to the rail, thereby reducing the power consumption of the carrier. Nevertheless, since the linear motor method employed remains consistent, the manufacturing costs and the complexity of the driving technique still exists.

Notably, linear motors offer a distinctive feature: the capability of planar motion. By employing 2 or more separate linear motors positioned perpendicularly within the same plane an additional motion axis can be introduced to the system [9–11]. This planar motion also can be achieved using perpendicular winding placement along the same motor yoke that is called planar motor [12]. Planar motors can also be utilised to simultaneously achieve levitation and propulsion of the carrier [13–17].

In the literature, Maglev carriers consist of many individual components, such as separate levitation units and thrust units [11]. A compact alternative solution is presented by Ahmed, Koseki and Kim [18]. While this approach employs a single unit to link levitation and thrust components, it is important to note that these components are still manufactured and assembled individually into the unit. Despite the advancements, this compact carrier and other 6 degrees of freedom (DoF) Maglev carriers still lack the degree of simplification desired. When evaluating all efficiency considerations, the reduction in the quantity of parts becomes crucial, as it leads to lowered manufacturing, maintenance, and operational costs, along with reduced energy consumption.

This study introduces an innovative hybrid linear actuator design aimed at simplifying the intricacies associated with planar Maglev carriers. The proposed actuator design, referred to as the "MaglevMotor", differs in terms of topology and control principles. The proposed MaglevMotor is a short-primary linear induction motor capable to levitate itself under a passive rail. Coupling both levitation and linear motion units in a singular yoke reduces the number of magneto-motor components by half, thereby leading to reduced manufacturing and maintenance costs and shrinks overall carrier dimensions. Besides the advantages of the Maglev technology and the novel coupled yoke structure, another feature of the MaglevMotor is that it allows modular usage. With the use of 3 MaglevMotors, 6 DoF motion can be achieved. Unlike the previous studies, carrying capacity of the carrier can be expanded by the number of MaglevMotor units used in the carrier by this modular structure.

The contribution of this study is the proposal of the levitating hybrid linear actuator named the MaglevMotor. The proposed hybrid actuator is designed to simplify the complexity associated with the current Maglev carriers, marked by a high number of parts and challenging assembly tolerances. Its hybrid structure enables the MaglevMotor to be controlled using the Zero Power Control algorithm for levitation, resulting in a substantial reduction in the power required for stable levitation. Additionally, the linear motor windings in the MaglevMotor allow for the generation of thrust force using the same yoke. The primary objective of this study is to propose an optimal yoke design by multi-physics multi-objective optimisation technique. Multi-objective optimisation is the general name of the optimisation method aiming to generate pareto optimal points for given multiple optimisation criteria [19]. For this study, these optimisation criteria are such as minimising total mass, maximising acceleration properties at 5 mm levitation air gap clearance, and minimising mechanical deformation of the yoke. In search of the optimal design magnetic flux density inside the yoke is constrained to not exceed 0.7 T. Since the total mass and the deformation of the yoke are mechanical parameters and acceleration and levitation forces are magnetic parameters, this mixed optimisation is called multi-physics optimisation. The optimisation process is divided into two phases: pre-optimisation studies and optimisation studies. This division allows for a faster and more straightforward implementation of the optimisation, as it is presented step by step. Initially, number of windings and winding type of linear motor are determined via iterative 3D finite element method (FEM) analyses with a reference geometry in pre-optimisation phases. Subsequently, 3D FEM analyses are performed with geometrical variables of the yoke to be optimised to obtain Design of Experiment (DoE) dataset. Those results of analyses are used to generate the surfaces of Response Surface Method (RSM) that emulates the system characteristics. Lastly, the Multi Objective Genetic Algorithm (MOGA) is applied to achieve optimal solution for this design. The results at each step are presented in corresponding chapters and conclusion is gathered to summarise this study. A flow chart of the optimisation process is given in Figure 1.

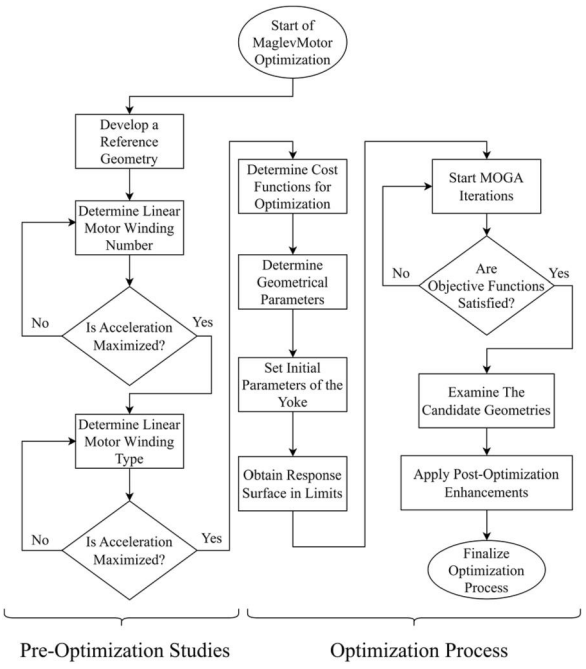


FIGURE 1 Flow chart of the optimisation process.

17518679, 0, Downloaded from https://ietresearch.onlinelibrary.wiley.com/doi/10.1049/elj2.12424 by Turkey Cochrane Evidence Aid, Wiley Online Library on [29/02/2024]. See the Terms and Conditions (https://onlinelibrary.wiley.com/terms-and-conditions) on Wiley Online Library for rules of use; OA articles are governed by the applicable Creative Commons License

Following the optimisation process, MaglevMotor units are manufactured and subjected to relevant experimental tests to ascertain the reliability and accuracy of the performance predictions derived from FEM analyses.

2 | MAGLEVMOTOR

2.1 | Proposal of the MaglevMotor and definitions of analyses

In literature, the definition of "Maglev motor" is used for levitating-shaft rotary motors. This technique proposes a mechanical levitating-shaft controlled in 5 DoF to pump blood in ventricular assist device [20]. In another study, the Maglev motor definition is used by Wang et al. In Wang's study, a 6 DoF motor is proposed using electrodynamic levitation; the motor has active PCB stator and passive Halbach magnets on mover [13]. The proposed hybrid linear actuator diverges in terms of both topology and objectives. Consequently, to avoid any potential confusion, the unified name "MaglevMotor" is introduced. Figure 2 illustrates the optimised MaglevMotor, which has been modelled within a computer-aided design (CAD) environment.

The components of the MaglevMotor presented in Figure 2 are as follows; the novel optimal yoke design (1), levitation control coils (2), permanent magnets (3), magnet covers (4), linear motor windings (5), and the assembly bracket (6). The yoke functions as the central electromagnetic component, while levitation control coils ensure stable levitation. Permanent magnets play a crucial role in both reducing levitation energy consumption and enabling the implementation of a zero-power controller. Additionally, protective magnet covers safeguard the permanent magnets from potential impacts. Linear motor windings are responsible for generating the thrust force, and the assembly bracket is employed to securely mount MaglevMotor unit onto the carrier's structure.

The MaglevMotor operates under passive planar rail. The rail acts as the secondary for MaglevMotor consists of two plates: the first one is an 8 mm thick back iron, and the second one is a 1 mm thick copper plate. Figure 3 represents the force components affecting MaglevMotor with the linear motor secondary.

F_A and $F_{A'}$ are attraction forces, F_T is the longitudinal propulsion force, and G is the gravitational force. F_A is generated by electromagnets and the permanent magnets placed on top of yoke poles, $F_{A'}$ and F_T are generated by energising the linear motor windings. Detailed explanation of the forces is given in following section.

At the beginning of this study, a reference geometry is established upon prior studies [21]. The process of scaling is executed by adjusting the attraction force of the preceding design to align with the newly targeted mass. The dimensions of the reference yoke are presented in Figure 4. For scaling purposes, the pole top cross-section area is designated as 400 mm^2, while the yoke cross-section is determined to be 200 mm^2 based on the applied scaling factor.

In Figure 4, a widened pole top profile with narrower yoke arms is presented. This method contributes to the reduction of the total mass of yoke [22]. The wider permanent magnet is placed on pole top profile, and dimensions are given. The number of slots of linear induction motor part is determined by pre-optimisation studies. The dimensions of the yoke and the permanent magnets are optimised in optimisation. The analyses types and correlative results are explained in relevant chapters.

2.2 | Pre-optimisation studies and fundamentals

Design and optimisation of the linear motors and Maglev systems have been studied by many researchers. Among the optimisation methods, the FEM-based optimisation approach

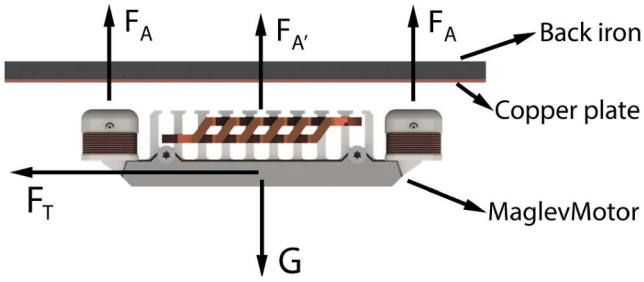


FIGURE 3 MaglevMotor force components under rail-passive track.

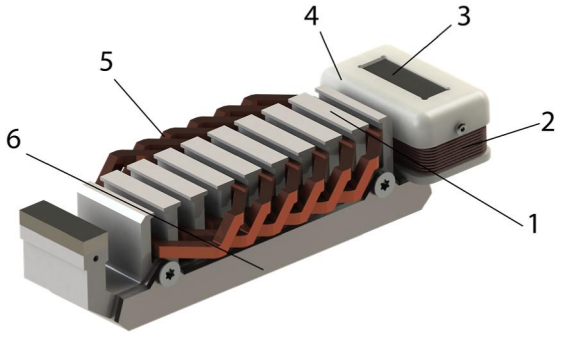


FIGURE 2 MaglevMotor components (one of the levitation coil and its cover are hidden).

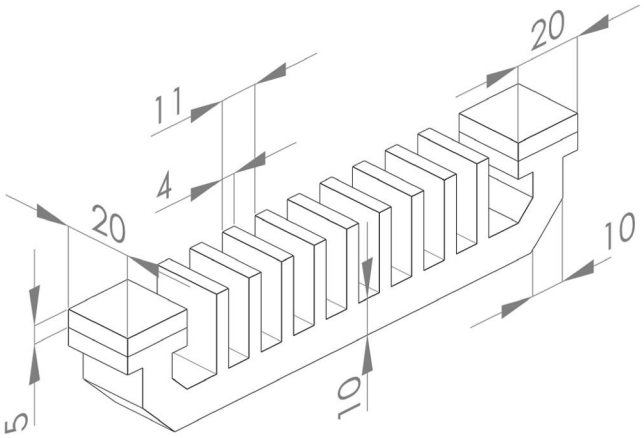


FIGURE 4 Reference dimensions of the yoke and the magnets.

17518679, 0, Downloaded from https://ietresearch.onlinelibrary.wiley.com/doi/10.1049/elp2.12424 by Turkey Cochrane Evidence Aid, Wiley Online Library on [29/02/2024]. See the Terms and Conditions (https://onlinelibrary.wiley.com/terms-and-conditions) on Wiley Online Library for rules of use; OA articles are governed by the applicable Creative Commons License

offers numerous advantages, notably the capability to optimise designs without requiring an exact analytical model. This proves particularly beneficial in cases where creating a comprehensive model becomes complex and challenging [23, 24].

Pre-optimisation studies are carried out to determine linear induction motor topology, such as winding type and number of windings. To ensure the highest accuracy, these preliminary analyses are executed using a 3D analysis approach in Ansys Electronics Desktop software. While 2D FEM analysis provides faster outcomes, its accuracy is limited by the absence of the 3rd dimension. Additionally, 2D analyses amplify the computed force based on model depth, inadvertently neglecting the impact of geometrical ratio effects. This underscores the necessity of employing a 3D approach.

In the initial phase of pre-optimisation studies, it is imperative to examine the forces and their consequential impacts on the system. The configuration illustrated in Figure 3 distinguishes itself from linear induction motors that operate with pure conductor plates, as seen in applications like Hyperloop [25]. In the context of Hyperloop technology and analogous systems, linear induction motors generate a repelling force on pure conductor rails, utilised for the levitation of systems a phenomenon known as electrodynamic levitation. In contrast, MaglevMotor and similar applications, termed electromagnetic levitation, employ attraction forces for levitation. Due to the presence of back iron, the eddy current induced by the linear motor and the resultant suspension forces manifest not as repelling forces but as attraction forces. Consequently, this attraction force introduces disturbances to stable levitation control. The mitigation of this undesired attraction force holds significant importance. The initial step involves an examination of the force outputs of the linear motor across a range of operable frequency values. The frequency response analyses are conducted on reference design, from 10 to 210 Hz excitation. The thrust force and attraction force outputs for standstill actuator are presented in Figures 5 and 6 respectively.

As observed in Figure 5, the attraction force experiences a significant reduction with an increase in frequency, indicating that higher frequencies are advantageous for the intended operation. Concurrently, the thrust force given in Figure 6 exhibits an increment with rising frequency, emphasising the preference for higher frequencies. Despite the fact that ~170 Hz appears to yield the highest thrust force, the increase in the driving frequency is limited by gate drivers. Taking into account the constraints of the driver circuit, and aiming for a disturbance attraction force lower than the targeted %10 of the required total carrier levitation force, a frequency of 100 Hz is deemed sufficient. At this selected frequency, the attraction force remains relatively low, while the thrust force reaches an acceptably high level. Subsequent analyses are carried out with the chosen frequency of 100 Hz.

The subsequent stage in pre-optimisation studies involves determining the motor length in conjunction with the winding number. In this study's context, a winding encompasses one coil per phase, totalling three coils for a three-phase motor. The use of pole number or pole pair number definitions is avoided in this context due to the fact that, for linear motors with constant slot and tooth dimensions, the pole number does not impact the output velocity. Within this framework, two windings signify two individual coils per phase, culminating in a total of six coils for the three-phase motor, and so forth. Consequently, thrust force analyses are conducted for configurations involving 1, 2, 3, and 4 number of windings. Figure 7 represents the concept of number of windings.

However, increasing number of windings increases phase resistance and inductance values proportionally. The resistance of each coil is calculated from Equation (1) and the inductive

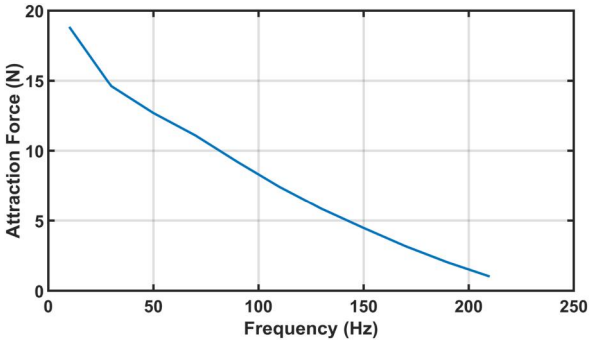


FIGURE 5 Attraction force at various frequency values.

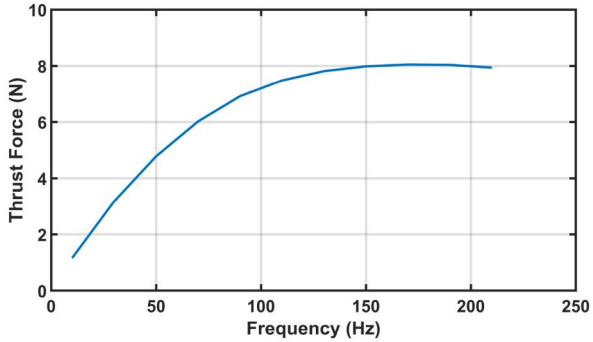


FIGURE 6 Thrust force at various frequency values.

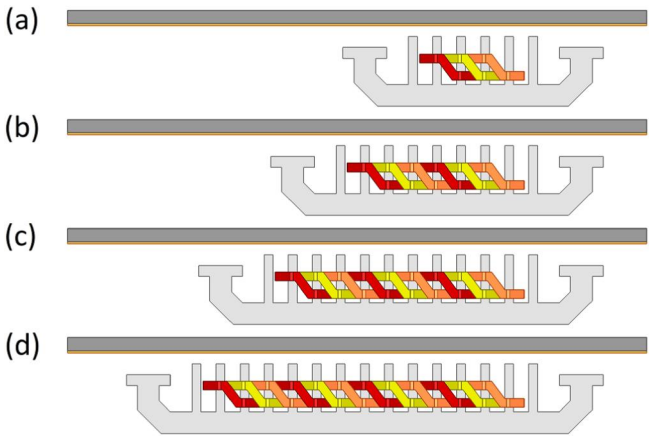


FIGURE 7 Number of windings; 1 winding (a), 2 windings (b), 3 windings (c), and 4 windings (d).

17518679, 0, Downloaded from https://ietresearch.onlinelibrary.wiley.com/doi/10.1049/elp2.12424 by Turkey Cochrane Evidence Aid, Wiley Online Library on [29/02/2024]. See the Terms and Conditions (https://onlinelibrary.wiley.com/terms-and-conditions) on Wiley Online Library for rules of use; OA articles are governed by the applicable Creative Commons License

reactance of each coil is calculated from Equation (2) with the dimensions of reference geometry.

$$R = \frac{\rho \cdot l_C}{A_C} \tag{1}$$

$$X_L = 2 \cdot \pi \cdot f \cdot \frac{\mu \cdot N^2 \cdot S_L}{l_L} \tag{2}$$

$$Z = \sqrt{R^2 + {X_L}^2} \tag{3}$$

The parameters of the equations above are: R is the resistance of the coil (Ω), ρ is the resistivity (Ω.m), l_C is the conductor length (m) and A_C is the cross-section area of the conductor (m^2). X_L is the inductive reactance (Ω), f is the frequency of alternating current (Hz), μ is the permeability of the yoke material, S_L is the cross-section area of the wounded coil (m^2) and l_L is the length of the coil (m). Applying Equations (1–3), the impedance (Z) of an individual coil is computed as 1 Ω, considering a presumed operational frequency of 100 Hz.

Therefore, the carrier proposed in this study is designed to operate within the constraints of a battery pack with limited voltage and current resources. Specifically, it is configured to be powered by an 11S2P lithium-ion battery pack, utilising cells with a maximum continuous current capacity of 10 A. According to those specifications, the practical maximum voltage value is 46.2 V and the maximum output current is 20A. Table 1 shows excitation limits conducted from battery unit for each number of windings respectively. The power provided in the table represents the input DC bus power.

With the given excitation values in Table 1, 3D transient thrust force analyses are carried out for the reference design. Ansys Electronics Desktop software uses average virtual force method to calculate the force, given in Equation (4).

$$F_{AV} = \frac{1}{2\pi} \int_0^{2\pi} \left(\frac{dW(s,i)}{ds} \right) d\omega t$$
$$W = \int_0^i \lambda(i) di \tag{4}$$

where F_{AV} is the average force, and W is the magnetic coenergy. λ is the flux linkage. The different number of windings analyses conducted and the thrust force results are given in Figure 8.

The Figure 8 reveals that even with lower input power, the 3 windings motor outperforms 2 windings motor. However, the thrust force comparison alone is not a reliable method to determine optimal design. Adding more windings and expanding the motor length results increase the mass of the motor and the mass of the entire carrier structure proportionally. In order to make the correct comparison, different geometries and topologies should be compared against a common performance criterion. One of the performance comparison parameters can be addressed as acceleration, as acceleration depends on both the output force and the mass. The subsequent comparison is carried out to evaluate the performance differences of self-accelerating four motors. Figure 9 verifies that the 2 windings motor which has lower thrust force can outperform the 3 windings motor in a manner of acceleration. According to these results, acceleration

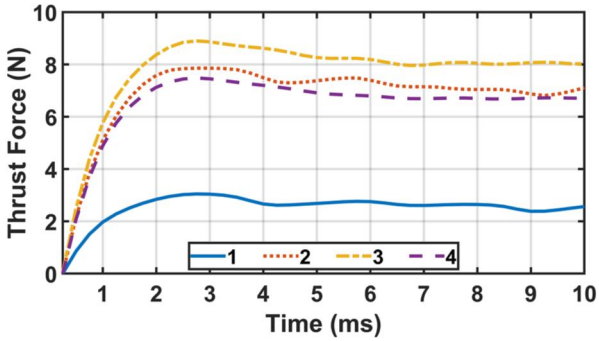


FIGURE 8 Thrust forces of motors with different number of windings.

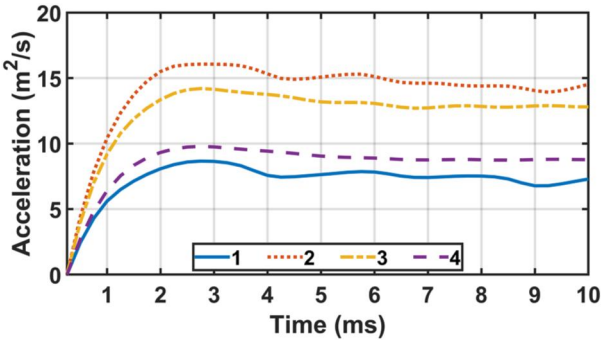


FIGURE 9 Accelerations of motors with different number of windings.

TABLE 1 Number of windings excitations and corresponding limits.

# of windings	Voltage (V)	Current (A)	Input power (W)	Limit type
1	20.0	20.0	400.0	Current limit
2	40.0	20.0	800.0	Current limit
3	46.2	15.4	711.5	Voltage limit
4	46.2	11.5	531.3	Voltage limit

17518679, 0, Downloaded from https://ietresearch.onlinelibrary.wiley.com/doi/10.1049/elj2.12424 by Turkey Cochrane Evidence Aid, Wiley Online Library on [29/02/2024]. See the Terms and Conditions (https://onlinelibrary.wiley.com/terms-and-conditions) on Wiley Online Library for rules of use; OA articles are governed by the applicable Creative Commons License

comparison gives more accurate results. Due to the accuracy described, the following performance measurements and comparison are made by acceleration analyses.

The principle of kinetic energy dictates that the energy required to move an object increases as its mass increases. In the case of a battery-powered carrier, the onboard power supply is subject to limitations. Therefore, it is advantageous to minimise the mass of the carrier, as this enhances operational duration and improves the acceleration and deceleration performance. To achieve the lowest possible mass, even if they exhibit nearly identical acceleration characteristics, the motor with 2 windings is the more favourable choice.

In the secondary phase of the pre-optimisation studies, iterative FEM analyses are carried out to determine the optimal winding type for the linear induction motor part. Linear induction motor synchronous speed is given in Equation (5) [26].

$$v_s = 2\tau f_s \tag{5}$$

where v_s is the speed of the translational motion (m/s), τ is the pole pitch (m) and f_s is the electrical frequency (Hz). Higher travel speed can be achieved by longer pole pitch under condition of equal supply frequency.

Two different winding types are examined: fractional and full-pitch. Fractional winding improves the output force characteristics by reducing the thrust force fluctuation [26]. Full-pitch winding results in higher speed and thrust force due to the longer pole pitch. Comparative analyses are performed for both designs by 20A excitation for 2 windings. Winding types are presented in Figure 10 and analyses results are given in Figure 11. Each phase is coloured differently for easier examination and comparison.

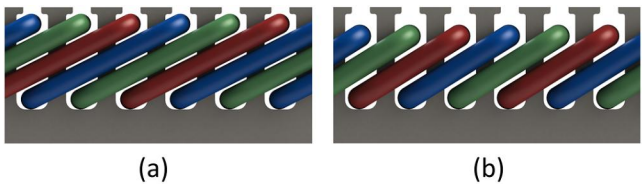


FIGURE 10 Winding types: full-pitch winding (a) and fractional pitch winding (b).

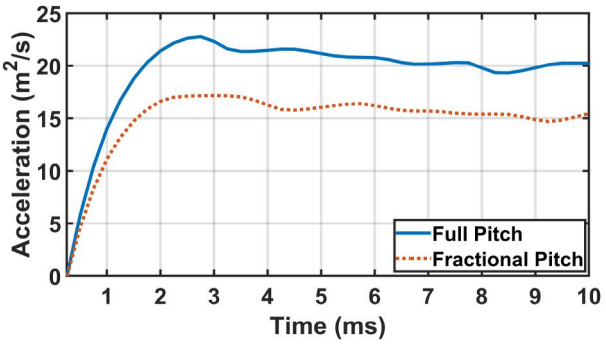


FIGURE 11 Acceleration comparison of fractional and full pitch winding types.

Figure 11 states that the motor with full pitch winding has higher acceleration capability than the motor with fractional winding. The decision to neglect force fluctuation was made in favour of prioritising advantages of improved acceleration and maximum speed.

In conclusion, pre-optimisation analyses indicate that full-pitch 2 windings motor is the optimal solution. Further geometrical optimisation steps for yoke geometry are given in the next chapter.

3 | MULTI OBJECTIVE MULTI PHYSICS OPTIMISATION

3.1 | Fundamental of optimisation technique

In this study, a multi-objective metaheuristic optimisation approach based on the FEM is implemented. Unlike single-objective optimisation methods, multi-objective optimisation methods yield Pareto optimal results. These results are not aimed at achieving global optimisation, as it is rarely possible to reach the utmost optimal point for each and every objective [19]. In this study, the number of geometrical parameters are set to the minimum for fast and accurate optimisation. It is evident that the dimensions of the linear motor's teeth and slot openings impact magnetic flux density, which is realised through iterative FEM analyses to avoid saturation. The influencing geometrical parameters include permanent magnet dimensions, yoke width, and yoke thickness, and their corresponding effects are provided in the following sections.

The primary objectives are to maximise acceleration, minimise mass, reduce mechanical deformation, and minimise stress, all while maintaining a 5 mm air gap at the levitation point and ensuring the yoke remains magnetically unsaturated. Optimisation is carried out in Ansys Workbench software. The optimisation steps are given in Figure 12. The steps are as follows; define the geometrical parameters of the yoke to be optimised, acquire DoE data matrix within limits of

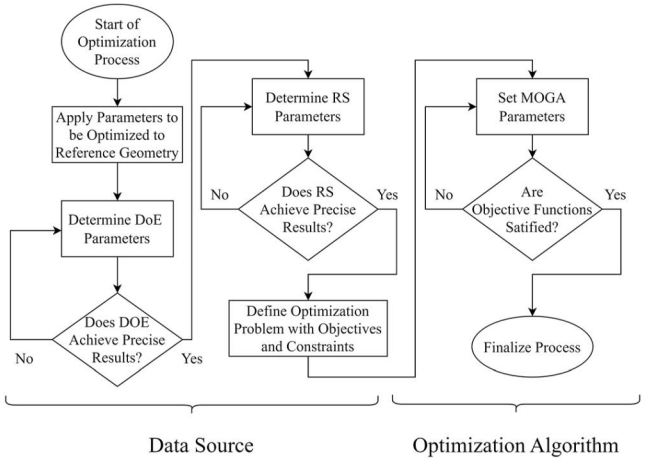


FIGURE 12 Detailed optimisation process steps.

17518679, 0, Downloaded from https://ietresearch.onlinelibrary.wiley.com/doi/10.1049/elj2.12424 by Turkey Cochrane Evidence Aid, Wiley Online Library on [29/02/2024]. See the Terms and Conditions (https://onlinelibrary.wiley.com/terms-and-conditions) on Wiley Online Library for rules of use; OA articles are governed by the applicable Creative Commons License

geometrical parameters and perform required FEM analyses, apply RSM to establish relationships between geometrical parameters and output variables, define optimisation goals and constraints, run optimisation algorithm, confirm pareto results.

The optimisation process on the reference design was commenced by associating the optimisation variables with the corresponding geometric dimensions. Figure 13 states the relevant dimensions along with their corresponding equations on the reference yoke.

where L_W is the width of the yoke (mm), L_M is the magnet length adjustment factor and L_T is the yoke thickness adjustment factor. Modified reference geometry implemented in a manner of predefined cross section areas of both yoke arm and permanent magnets. As mentioned before, magnet cross section is predefined to be 400 mm^2 and yoke arm width to be 200 mm^2. To accommodate the optimisation parameters, those adjustment variables are defined and added to equations of the predefined geometric ratios.

3.2 | Design of Experiment and Response Surface Method

Finite element method analyses, employing high quality mesh and non-linear material libraries, provide precisely accurate results. Unlike analytical models that often make assumptions and neglect uncertain parameters or effects, FEM analyses can foresee all parameters and effects if configured correctly. However, this method requires a lot of computation time and uses high computation power. Those weaknesses limit the number of FEM analyses to be conducted due to resource limitations.

The study employs the RSM in conjunction with a DoE to overcome these limitations. The DoE is employed to systematically map input parameters within predefined user-defined limits. The design variables and their respective limits are outlined in Table 2.

In this study, *Enhanced Face-Centred Central Composite Design* type DoE mapping is employed. This method maps input parameters to 5 points each; covering middle, maximum and minimum absolute limits, and fractions of both limits. As an illustrative example, as given in Table 2, limits of L_W parameters are set at 15 and 45 mm. The L_W parameter is then mapped as *[15 22.5 30 37.5 45]*. This approach, incorporating additional fractional steps, enhances accuracy by leveraging a greater amount of real data gathered in analyses to improve the surface modelling process.

Each 3D FEM analysis required approximately 27 min to complete. A total of 29 points is analysed to gather DoE dataset, which takes slightly more than 13 h. PC configuration used in analyses is: i7 7700HQ 4/8 core CPU and 16 GB RAM.

Although the DoE yields relatively precise system characteristics at the data points, it exhibits discontinuity. To achieve continuous relations between parameters, RSM is adopted. Surfaces are obtained by *Full 2nd Order Polynomial* method. As an example, in Figure 14, the response of magnetic flux density to geometric parameters is given. The results shows that the response surface has the ability to mimic system properties. As expected, increasing the magnet size and decreasing the yoke cross-section area increases the flux density.

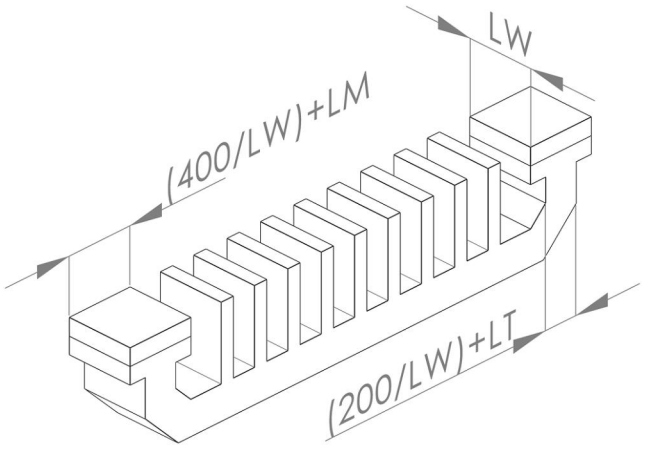


FIGURE 13 Geometric dimensions of the yoke with associated optimisation parameters.

TABLE 2 Geometric variables of optimisation.

Parameter	Definition	Minimum (mm)	Maximum (mm)
L_W	Yoke width	15	45
L_T	Yoke thickness adjustment	−3	3
L_M	Magnet length adjustment	−5	5

3.3 | Multi objective genetic algorithm

In this study, optimisation based on FEM is carried out using the MOGA. Genetic algorithm is a stochastic optimisation method mimics biological generation development with selection, crossover, and mutation processes. Every generation approach to the optimal solution step by step and random mutation and crossover processes increase robustness of

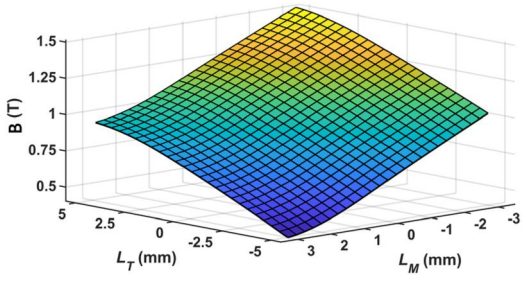


FIGURE 14 Response of magnetic flux density to L_T and L_M.

17518679, 0, Downloaded from https://ietresearch.onlinelibrary.wiley.com/doi/10.1049/elj2.12424 by Turkey Cochrane Evidence Aid, Wiley Online Library on [29/02/2024]. See the Terms and Conditions (https://onlinelibrary.wiley.com/terms-and-conditions) on Wiley Online Library for rules of use; OA articles are governed by the applicable Creative Commons License

population [19]. This method can be used to achieve optimal solution for multiple objectives [27].

Ansys software computes "*Non-dominated Sorted Genetic Algorithm-II*" for optimisation. This method gives opportunity to achieve optimal solution faster than traditional Pareto ranking methods. The MOGA algorithm first generates the initial population, than generates a new population via cross-over and mutation. After a converged solution obtained, optimisation algorithm runs again by the number of iterations to validate the solution.

After gathering the response surfaces, which is the main time-consuming part of the process because of the data of FEM analyses of DoE, the subsequent optimisation phase can be completed significantly faster. Using the same PC configuration, MOGA takes approximately 30 s. This can be attributed to the relatively low volume of data to process, such as 29 data sets are enumerated in optimisation phase opposing thousands of mesh points calculated step by step in FEM analyses. This fast operation gives opportunity to test various algorithms and algorithm parameters much faster. Summary of cost functions are given in Table 3.

Cost functions and corresponding definitions are given in Equations (6) to (9).

$$F(X) = [f_1(X)\ f_2(X)\ f_3(X)]^T$$

$$\begin{cases} f_1(X) = \min(M) \\ f_2(X) = \min(\delta) \\ f_3(X) = \max(A_L) \end{cases} \tag{6}$$

$$X = [L_W\ \ L_T\ \ L_M]^T$$

$$X_L \le X \le X_U$$

where M is the total mass (kg), δ is the deformation (mm) and A_L is the longitudinal acceleration (m/s^2). X is the matrix of geometrical parameters stated in Figure 12. In the MOGA setup, each objective is defined individually. Consequently, cost functions formulated for each objective, resulting in 3 individual functions. Descriptions of each function is provided in the following paragraphs.

Minimising the total mass, $f_1(X)$: Total mass is calculated by summing each individual component, with an additional 10% of a single MaglevMotor's mass included to account for assembly components along with 5 kg of mass added for the masses of base, battery, sensors, and electronic components. All values are in (kg). Minimising mass is dependent on all the optimisation parameters.

Minimising the deformation of the yoke, $f_2(X)$: The deformation of yoke is related to attraction force and cross-section area of yoke. The relations of input and output parameters are given in Equation (7). Deformation is dependent on all optimisation parameters.

$$\begin{aligned} f(\delta) &\approx F_A/A_Y \\ f(F_A) &\approx L_W, L_M \\ A_Y &\approx L_W, L_T \end{aligned} \tag{7}$$

where F_A is the attraction force (N) and A_Y is the cross-section area of the yoke (m^2).

Maximising the longitudinal acceleration, $f_3(X)$: The longitudinal acceleration and corresponding optimisation parameters are given in Equation (8). Acceleration is primarily affected by the LW parameter, but it is worth noting that the total mass also plays a significant role in the motor's performance. In conclusion, the acceleration cost function depends on all optimisation parameters.

$$\begin{aligned} f(A_L) &= F_T/M \\ f(F_T) &\approx L_W \cdot A \\ A &\approx 1/L_W \end{aligned} \tag{8}$$

where F_T is the longitudinal thrust force (N), and A is the excitation current (A).

Following the definition of the optimisation cost functions, constraints are determined and detailed in Table 4. These constraints are chosen based on material limitations and operational point selection criteria.

The zero power condition, denoted as f_{zpc}, represents the state of aiming to achieve the levitation force (attraction force) equal to gravitational force. Zero power condition function dependent on L_W and L_M assuming yoke is not saturated. The second constraint B is the magnetic flux density within the yoke (T). B is dependent on all the optimisation parameters.

The functions corresponding to the optimisation constraints are given in Equation (8). Zero power condition intended to approach to 1 and limited to upper and lower values 1.1 and 0.9 respectively. Similarly, B is intended to approach to 0.8 T and limited to 0.7 T minimum. Parameters of used MOGA are given in Table 5, which are selected or calculated by the software automatically.

TABLE 3 Goal parameters of optimisation.

Parameter	Definition	Goal	Priority
M	Total mass	Minimise	High
A_L	Longitudinal acceleration	Maximise	High
δ	Mechanical deformation	Minimise	Default

TABLE 4 Optimisation constraints.

Parameter	Definition	Lower	Upper	Goal	Priority
f_{zpc}	Zero power condition	0.9	1.1	1	Default
B	Magnetic flux density	0.7	-	0.8	Default

17518679, 0, Downloaded from https://ietresearch.onlinelibrary.wiley.com/doi/10.1049/elp2.12424 by Turkey Cochrane Evidence Aid, Wiley Online Library on [29/02/2024]. See the Terms and Conditions (https://onlinelibrary.wiley.com/terms-and-conditions) on Wiley Online Library for rules of use; OA articles are governed by the applicable Creative Commons License

$$G(X) = [g_1(X)\ \ g_2(X)]^T$$

$$s.t. \begin{cases} g_1(X) = f_{zpc} = F_A/(M_T \cdot 9.81) = 1 \\ g_2(X) = B = 0.8 \end{cases} \quad (9)$$

$$0.9 < g_1(X) < 1.1$$

$$0.7 < g_2(X)$$

The MOGA optimisation converges by 70% Pareto percentage and 11.8% stability percentage. The results including corresponding optimised geometric parameters are given in Table 6 for mechanical values, levitation parameters, thrust parameters and mechanical parameters in the following order.

Table 6 provides an overview of the input parameters, candidate optimal points, and a user-defined manufacturable point that considers manufacturing constraints such as integer dimensions for permanent magnet sizes. The results indicate that, in the first three rows, the yoke should be slightly thicker, the magnets should be smaller compared to the reference design, and the width should be around 30 mm to achieve the specified objectives. According to these results, each candidate meets the required goals. Figure 15 presents a magnetic flux density graph for the user specified design, demonstrating that the magnetic flux density remains within design limits for static analyses, indicating that the optimisation of the MaglevMotor is satisfactory.

Similarly, the mechanical stress analyses results indicate that in all candidate points stress values are well below the material limits. These results suggest that the yoke width is constrained primarily by the magnetic flux density rather than mechanical limits. Total deformation graph is given in Figure 16.

The final optimised MaglevMotor dimensions are given in Figure 17.

After completing the optimisation process, final enhancements are applied to the design. One notable enhancement involves the tooth tip, which serves to lower magnetic reluctance and improve the motor performance. However, it is worth noting that this profile extension is limited due to the potential leakage of magnetic flux from tooth to tooth. When the slot opening is too small (i.e. smaller than the motor's air gap), it can increase the magnetic flux leakage, subsequently reducing both the output force and efficiency. Table 7 presents a three-step comparison of different tooth tip dimensions in various air gap analyses. The iterative 3D FEM analyses were conducted to identify the optimal extension range that results in the highest thrust.

TABLE 5 Multi objective optimisation parameters.

Parameter	Value
Number of initial samples	3000
Number of samples per iteration	600
Maximum number of iteration	20
Maximum allowable pareto percentage	70
Convergence stability percentage	2
Crossover probability	0.98
Mutation probability	0.01

TABLE 6 Optimisation results.

Parameter\No candidate	No. 1	No. 2	No. 3	User
Width (mm)	33.4604	32.0850	30.6046	30.0000
Magnet Length Adj. (mm)	−2.6204	−2.9134	−3.3106	−3.3333
Yoke Thickness Adj. (mm)	0.7431	0.8309	0.1807	1.0000
Yoke Mass (kg)	1.0605	1.0451	0.9949	1.0236
Total Mass (kg)	8.4997	8.4488	8.2832	8.3777
Attraction force (N)	28.0412	27.6506	26.4991	27.2889
Zero power ratio	0.9948	0.9862	0.9647	0.9814
Flux density (static) (T)	0.7707	0.7409	0.7986	0.6978
Thrust force (N)	18.6097	18.1526	17.3903	17.3429
Single accel. (m/s^2)	1.7888	1.7706	1.7818	1.7272
Total accel. (m/s^2)	0.2232	0.2190	0.2140	0.2110
Flux density (motion) (T)	0.8971	0.8826	0.9177	0.8930
Equivalent stress (MPa)	0.8425	0.8302	0.8765	0.8166
Deformation (mm)	8.34E-05	7.86E-05	8.75E-05	7.57E-05

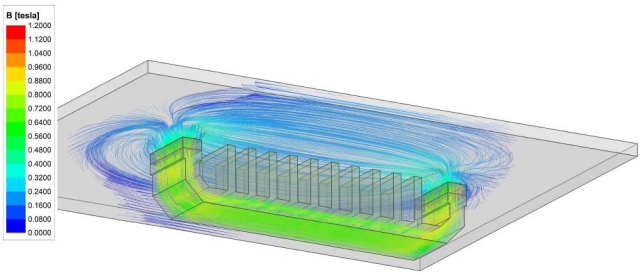


FIGURE 15 Magnetic flux density distribution of MaglevMotor.

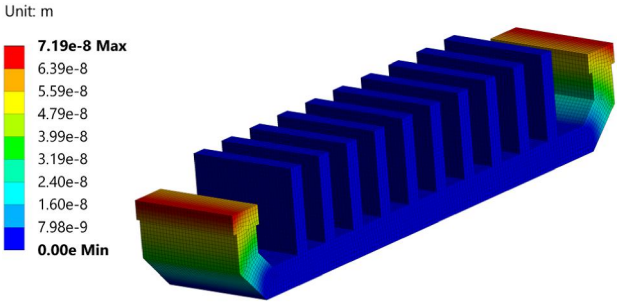


FIGURE 16 Deformation plot on the yoke.

17518679, 0, Downloaded from https://ietresearch.onlinelibrary.wiley.com/doi/10.1049/elp2.12424 by Turkey Cochrane Evidence Aid, Wiley Online Library on [29/02/2024]. See the Terms and Conditions (https://onlinelibrary.wiley.com/terms-and-conditions) on Wiley Online Library for rules of use; OA articles are governed by the applicable Creative Commons License

Expanding the slot opening results in higher reluctance, directing magnetic flux from tooth to rail and back to corresponding return tooth, thereby preventing any short circuit between other teeth of the motor. The proposed Maglev carrier is designed to levitate using zero power control algorithm. 5 mm air gap selected for this study and design is realised around this selected point. However, when the carrier carries an external load, because of the zero power controller, it will levitate itself with a reduced air gap. In conclusion, the carrier's operational range begins at 5 mm and gradually decreases. Within this defined range of motion, the choice of a 1.5 mm extension for the teeth is deemed favourable.

4 | EXPERIMENTAL VERIFICATION

After achieving the optimal solution by iterative FEM analyses and optimisation algorithm, experimental studies are carried out to verify results. To verify the optimisation results, two separate test setups utilised to measure the attraction force and the thrust force. Firstly, as illustrated in Figure 18, the MaglevMotor placed on an aluminium rod is used to adjust the air gap. Then force measurements were carried out for each air gap value with excitation current values. The experimental results and FEM results are given in 3D graphs in Figures 19 and 20 for comparison and error analysis in order. The results are notably consistent.

Difference in the data can be attributed to various factors, including the relatively low resolution of the strain gauge, deformations in assembly parts, and partial magnetisation of the rail. Consequently, while the force graphs exhibit similar characteristics along the excitation axis, the observed differences may be attributed to variations in permanent magnet quality and other contributing factors. Interestingly, shifting the data by 1 mm results in an acceptable match between the experimental and FEM data, with an error margin of approximately 10%.

The second experiment is conducted to verify the thrust force. Figure 21 presents the setup of the thrust force measurement.

A semi-rail platform is utilised to provide required motion freedom to measure the thrust force of MaglevMotor. Ball bearing rollers on aluminium rail are used to minimise friction

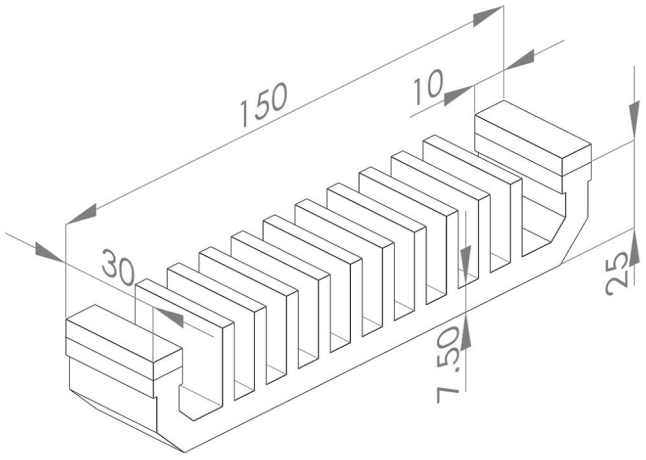


FIGURE 17 Optimised MaglevMotors yoke dimensions.

TABLE 7 Teeth tip dimension range for maximum thrust.

Air gap (mm)	Minimum extension (mm)	Maximum extension (mm)
2	1.5	2.0
5	1.0	1.5
8	0.5	1.0

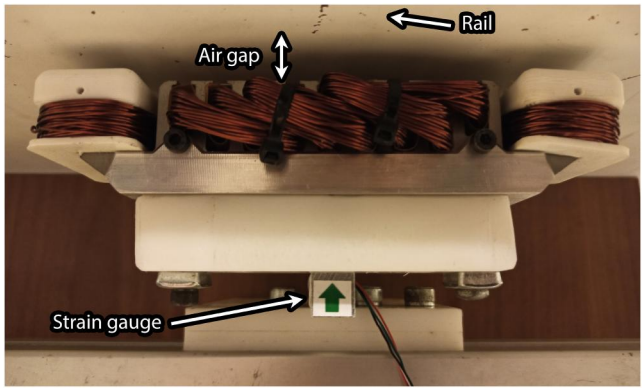


FIGURE 18 Experimental setup for attraction force measurements.

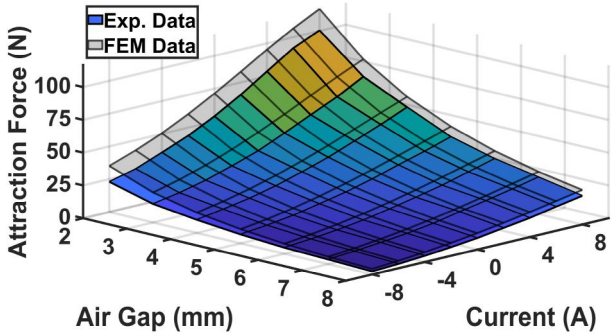


FIGURE 19 Attraction force comparison of experiment and finite element method (FEM).

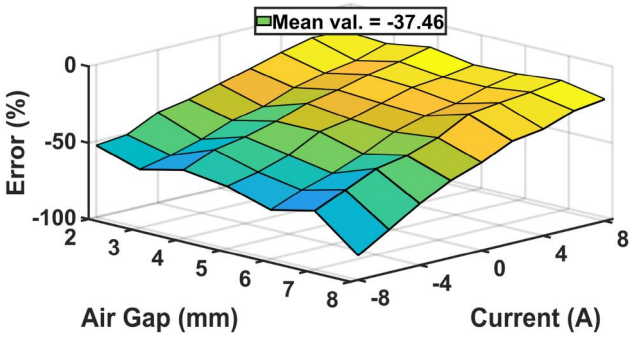


FIGURE 20 Error comparison of attraction forces.

17518679, 0, Downloaded from https://ietresearch.onlinelibrary.wiley.com/doi/10.1049/elp2.12424 by Turkey Cochrane Evidence Aid, Wiley Online Library on [29/02/2024]. See the Terms and Conditions (https://onlinelibrary.wiley.com/terms-and-conditions) on Wiley Online Library for rules of use; OA articles are governed by the applicable Creative Commons License

effects. Similarly, the air gap set within analysed range and excitation current is incrementally applied.

Experiment results with FEM comparison are given in Figures 22 and 23 for the thrust force and error in order. Similar to the first experiment, FEM analyses results are acceptable compared to real experiment data.

Figure 23 indicated that at low excitation currents and higher air gap values error increases. At high excitation current values and close to the operating air gap error is lower than 10% which is pleasurably acceptable.

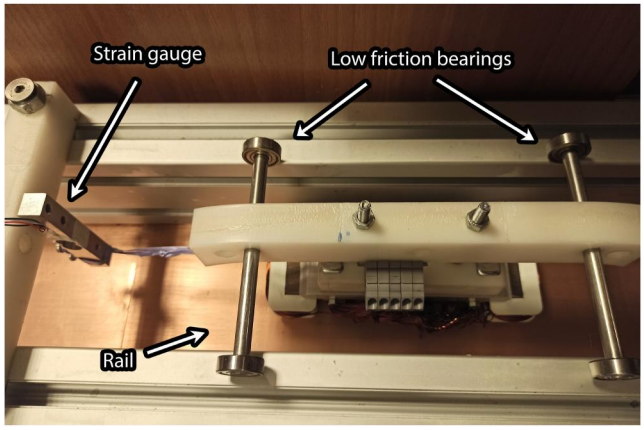


FIGURE 21 Experimental setup for thrust force measurements.

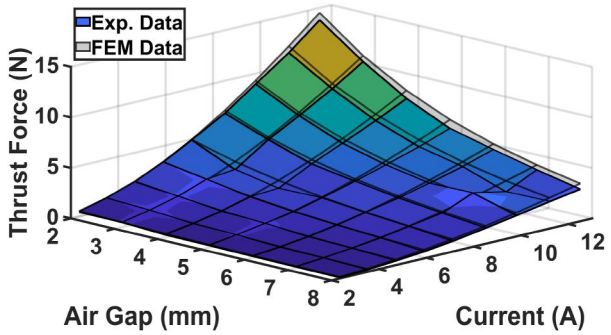


FIGURE 22 Thrust force comparison of experiment and finite element method (FEM).

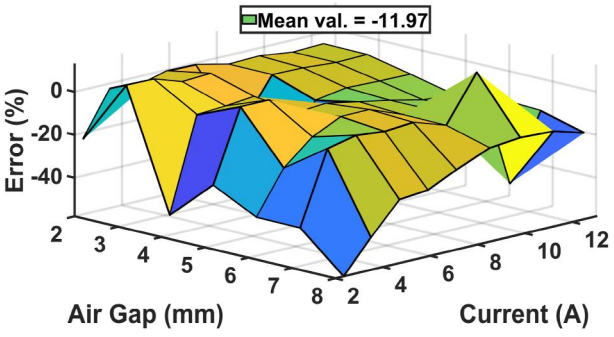


FIGURE 23 Error comparison of thrust forces.

5 | COMPLETE MAGLEV CARRIER

The whole Maglev carrier consists of 3 MaglevMotors, 3 position (air gap) sensors and base with mounting parts. MaglevMotors are placed 120° apart for symmetrical thrust distribution in both x and y axes. Also, each MaglevMotor admitted being symmetrically manufactured with same permanent magnets, they should also provide same attraction force at the same air gap. This triangular shape is balanced in terms of centre of mass which also balances levitation forces. Design of the whole carrier in CAD environment is given in Figure 24.

MaglevMotor placing can vary depending on the magnetic flux direction. Using those 3 hybrid yokes relatively close to each other causes an interesting phenomenon. Magnetic circuit completes its loop in a single line passing through all 3 yokes. The magnetic flux line graph is given in Figure 25.

Even though previous studies [18] have indicated that modelling each force point separately is sufficient for robust levitation of the system, analysis of coupled magnetic flux maps are examined. Figure 24 displays the distribution of magnetic flux density (B) in different scenarios. It is observed that the asymmetrical placement results in significantly higher magnetic flux density in the rail. Additionally, the magnetic flux lines turn back over the yoke length and form shortcuts during linear motion, leading to saturation of the yoke in the middle part and causing an asymmetrical distribution of force on the units. When the same part of the rail is used for both levitation and linear motion, it creates a conflict in the magnetic flux path



FIGURE 24 Proposed 6 degrees of freedom (DoF) MAGLEV carrier equipped with three MaglevMotor units.

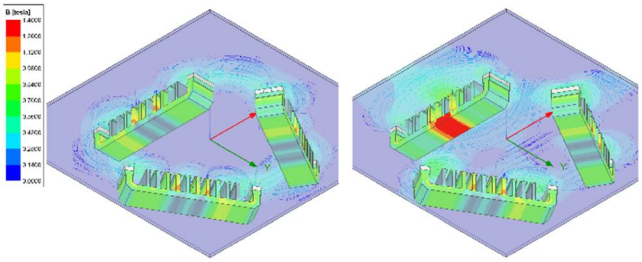


FIGURE 25 Magnetic flux density distributions of system using symmetrical (left) and asymmetrical (right) placement of three MaglevMotors.

17518679, 0, Downloaded from https://ietresearch.onlinelibrary.wiley.com/doi/10.1049/elp2.12424 by Turkey Cochrane Evidence Aid, Wiley Online Library on [29/02/2024]. See the Terms and Conditions (https://onlinelibrary.wiley.com/terms-and-conditions) on Wiley Online Library for rules of use; OA articles are governed by the applicable Creative Commons License

volume. To resolve this conflict, one could widen the rail thickness and yoke thickness, but this solution would increase the weight of both the railway and carrier, leading to higher overall costs. Consequently, symmetrical placement is chosen for its operational efficiency and cost-effectiveness in both manufacturing and operation processes.

6 | CONCLUSION

This study presents the design details of a modular hybrid linear actuator, called 'MaglevMotor', intended for use in a mobile 6 DoF Maglev carrier system. In the FEM-based actuator design, the process is outlined in three stages: the preliminary development process, the optimisation process, and the post-optimisation process. This step-by-step approach describes the impact of linear motor winding number, winding type, and the yoke's dimensions on actuator performance. The optimisation process is carried out with an adequate number of geometric dimensions, and the constraints are chosen to address both the proposed actuator performance criteria and the overall optimisation process efficiency. The final design is capable of generating a thrust force of 17.34 N and achieving a self-acceleration of 1.72 m/s^2. The modular nature of this design allows for the use of varying numbers of MaglevMotor units depending on specific application requirements. For 6 DoF motion, three MaglevMotor units are employed in the carrier system. The mobile Maglev carrier has the capacity to transport an 8 kg payload with an approximate base mass of 8 kg. Using the NdFe35 magnets sized at 30 × 10 × 5 mm, the MaglevMotors can maintain a levitation distance of 5 mm. The maximum acceleration achieved by the carrier is 0.21 m/s^2. The sizes of the magnets and yoke dimensions were optimised using MOGA to achieve the most optimal design. The configuration and placement of MaglevMotors were analysed to achieve a feasible redundant multi-degree-of-freedom Maglev carrier. Finally, the proposed hybrid linear actuator, the MaglevMotor, was manufactured and its performance was experimentally validated. Throughout the study, the time-variant dynamics of the MaglevMotor, such as changing velocity and the corresponding slip ratio, are neglected. Similarly, despite the minimal eddy-current effects of levitation coils, their dynamic effects are not examined within the scope of this study. These aspects could be considered as secondary characterisation studies of the MaglevMotor, and potential future enhancements can be pursued.

In future work, coupling effects will be examined to enhance the modelling of the total system. The proposed MAGLEV carrier will be assembled, and levitation experiments will be studied. Following this, it is planned to implement efficiency parameter of the MaglevMotor to optimisation model.

AUTHOR CONTRIBUTION

Ahmet Fevzi Bozkurt: Conceptualisation; Investigation; Methodology; Project administration; Resources; Validation; Writing – original draft. **Kadir Erkan**: Supervision; Writing – review & editing.

ACKNOWLEDGEMENTS

This work was supported by the Council of Higher Education (YÖK) 100/2000 scholarship program, The Scientific and Technological Research Institution of Turkey (TÜBİTAK) 2211/A scholarship program and Yıldız Technical University Department of Mechatronics Engineering Laboratory and YTU Maglev Laboratory.

CONFLICT OF INTEREST STATEMENT

No.

DATA AVAILABILITY STATEMENT

Data available on request from the authors.

ORCID

Ahmet Fevzi Bozkurt https://orcid.org/0000-0002-2619-5526

REFERENCES

1. Meins, J., Miller, L., Mayer, W.J.: The high speed Maglev transport system TRANSRAPID. IEEE Trans. Magn. 24(2), 808–811 (1988). https://doi.org/10.1109/20.11347
2. Erkan, K., et al.: Experimental evaluation of zero-power levitation control by transfer function approach for a 4-pole hybrid electromagnet. In: 2011 IEEE International Conference on Mechatronics, pp. 23–28 (2011). https://doi.org/10.1109/ICMECH.2011.5971299
3. Demircali, A.A., et al.: Longitudinal motion modeling and experimental verification of a microrobot subject to liquid laminar flow. IEEE ASME Trans. Mechatron. 26(6), 2956–2966 (2021). https://doi.org/10.1109/TMECH.2020.3049069
4. Kim, W.: Six-axis nano-positioning with planar magnetic levitation. In: Proceedings of the 2001 1st IEEE Conference on Nanotechnology. IEEE-NANO 2001 (Cat. No.01EX516), pp. 174–179 (2001). https://doi.org/10.1109/NANO.2001.966414
5. Huang, S., et al.: Overview of linear motors for transportation applications. In: 2018 IEEE 27th International Symposium on Industrial Electronics (ISIE), pp. 150–154 (2018). https://doi.org/10.1109/ISIE.2018.8433682
6. McLean, G.W.: Review of recent progress in linear motors. In: IEE Proceedings B (Electric Power Applications) (1988). https://doi.org/10.1049/ip-b.1988.0042
7. Sawada, K.: Development of magnetically levitated high speed transport system in Japan. IEEE Trans. Magn. 32(4), 2230–2235 (1996). https://doi.org/10.1109/20.508609
8. Mihalachi, M., Mutschler, P.: Evaluation of two position acquisition systems for permanent magnet linear motors with passive movers. In: 2008 11th International Conference on Optimization of Electrical and Electronic Equipment, Brasov, Romania, pp. 37–44 (2008). https://doi.org/10.1109/OPTIM.2008.4602455
9. Kumagai, M., Hollis, R.L.: Development and control of a three DOF planar induction motor. In: 2012 IEEE Int. Conf. Robot. Autom. (2012). https://doi.org/10.1109/ICRA.2012.6224612
10. Dittrich, P., Radeck, D.: 3 - DOF planar induction motor. In: 2006 IEEE International Conference on Electro/Information Technology, pp. 81–86 (2006). https://doi.org/10.1109/EIT.2006.252173
11. Makino, Y., Kovudhikulrungsri, L., Koseki, T.: 6 degrees of freedom control through three electromagnets and three linear induction motors. In: Symp. On Power Electronics, Electrical Drives, Automation & Motion, SPEEDAM 2004, Paper No. 50, Jul-04, Italy (2004)
12. Pan, J.F., et al.: A novel planar switched reluctance motor for industrial applications. IEEE Trans. Magn. 42(10), 2836–2839 (2006). https://doi.org/10.1109/TMAG.2006.879143
13. Wang, L.-J., et al.: A new four-phase current distribution strategy for the novel 6-DOF maglev motor. In: 2021 13th International Symposium on

17518679, 0, Downloaded from https://ietresearch.onlinelibrary.wiley.com/doi/10.1049/elj2.12424 by Turkey Cochrane Evidence Aid, Wiley Online Library on [29/02/2024]. See the Terms and Conditions (https://onlinelibrary.wiley.com/terms-and-conditions) on Wiley Online Library for rules of use; OA articles are governed by the applicable Creative Commons License

Linear Drives for Industry Applications (LDIA), Wuhan, China, pp. 1–6 (2021). https://doi.org/10.1109/LDIA49489.2021.9505904
14. Kou, B., et al.: A real-time computation model of the electromagnetic force and torque for a maglev planar motor with the concentric winding. Appl. Sci. 7(1), 98 (2017). https://doi.org/10.3390/app7010098
15. Usman, I.-U.-R., Lu, X.: Force ripple attenuation of 6-DOF direct drive permanent magnet planar levitating synchronous motors. IEEE Trans. Magn. 51(12), 1–8 (2015). Art no. 8208708. https://doi.org/10.1109/TMAG.2015.2461611
16. Smeets, J.P.C., et al.: Design and experimental validation of a magnetically suspended planar motor with integrated contactless energy transfer system. In: 2015 IEEE International Electric Machines & Drives Conference (IEMDC), pp. 669–675 (2015). https://doi.org/10.1109/IEMDC.2015.7409131
17. Zhang, K., Xu, F., Xu, X.: Robust iterative learning model predictive control for repetitive motion of maglev planar motor. IET Electr. Power Appl. 16(10), 1189–1200 (2022). https://doi.org/10.1049/elp2.12213
18. Salman, A., Koseki, T., Kim, H.J.: Proposal of a compact magnetically levitated transverse flux permanent magnet linear synchronous motor as a 6-DOF transport carrier. J. Eng. 2019(17), 4420–4425 (2019). https://doi.org/10.1049/joe.2018.8140
19. Deb, K., et al.: A fast and elitist multiobjective genetic algorithm: NSGA-II. IEEE Trans. Evol. Comput. 6(2), 182–197 (2002). https://doi.org/10.1109/4235.996017
20. Osa, M., et al.: Compact maglev motor with full DOF active control for miniaturized rotary blood pumps. In: LDIA 2017 - 11th Int. Symp. Linear Drives Ind. Appl. (2017). https://doi.org/10.23919/LDIA.2017.8097234
21. Bozkurt, A.F., Et Al.: Multi degrees of freedom robust magnetic levitation control of a flexible transport mover with disturbance observer and state feedback control. CONTROL ENGINEERING AND APPLIED INFORMATICS 20(3), 50–59 (2018)
22. Bucak, M., et al.: A new design concept of magnetically levitated 4 pole hybrid mover driven by linear motor. In: 2017 IEEE International Conference on Robotics and Automation (ICRA), pp. 596–601 (2017). https://doi.org/10.1109/ICRA.2017.7989073
23. Mutluer, M., Bilgin, O.: Design optimization of PMSM by particle swarm optimization and genetic algorithm. In: 2012 International Symposium on Innovations in Intelligent Systems and Applications, pp. 1–4 (2012). https://doi.org/10.1109/INISTA.2012.6247024
24. Jiang, J., Jiang, Q., Xiao, S.: Electromagnetic optimization of single-sided linear induction motors based on the genetic algorithm; electromagnetic optimization of single-sided linear induction motors based on the genetic algorithm. In: 2019 Int. Conf. Intell. Comput. Autom. Syst. (2019). https://doi.org/10.1109/ICICAS48597.2019.00077
25. Ji, W.-Y., et al.: A study of non-symmetric double-sided linear induction motor for Hyperloop all-in-one system (propulsion, levitation, and guidance). IEEE Trans. Magn. 54(11), 1–4 (2018). Art no. 8207304. https://doi.org/10.1109/TMAG.2018.2848292
26. Grigsby, L.L.: The Electric Power Engineering Handbook: Electric Power Generation, Transmission, and Distribution, ed. CRC Press (2012)
27. Wu, S., Lu, Q.: Multi-objective optimization of the linear induction motor by a hybrid optimal strategy. In: 2021 13th International Symposium on Linear Drives for Industry Applications (LDIA), pp. 1–5 (2021). https://doi.org/10.1109/LDIA49489.2021.9505894

How to cite this article: Bozkurt, A.F., Erkan, K.: MaglevMotor: Design and optimisation of a novel hybrid linear actuator for 6 degrees of freedom rail-passive Maglev carrier. IET Electr. Power Appl. 1–13 (2024). https://doi.org/10.1049/elp2.12424

17518679, 0, Downloaded from https://ietresearch.onlinelibrary.wiley.com/doi/10.1049/elp2.12424 by Turkey Cochrane Evidence Aid, Wiley Online Library on [29/02/2024]. See the Terms and Conditions (https://onlinelibrary.wiley.com/terms-and-conditions) on Wiley Online Library for rules of use; OA articles are governed by the applicable Creative Commons License